

## Reconstructing Relativistic Magnetohydrodynamics with Physics-Informed Neural Networks

CORWIN CHEUNG,<sup>1,5</sup> MARCOS JOHNSON-NOYA,<sup>1,2</sup> MICHAEL XIANG,<sup>1,2</sup> DOMINIC CHANG,<sup>3</sup> AND ALFREDO GUEVARA<sup>4</sup>

<sup>1</sup>*Harvard College, Cambridge, MA 02138, USA*

<sup>2</sup>*Harvard John A. Paulson School of Engineering and Applied Sciences, 150 Western Avenue, Allston, MA 02134, USA*

<sup>3</sup>*Center for Astrophysics — Harvard & Smithsonian, 60 Garden Street, Cambridge, MA 02138, USA*

<sup>4</sup>*Institute for Advanced Study, 1 Einstein Drive, Princeton, NJ 08540, USA*

<sup>5</sup>*OpenAI, 1455 3rd Street, San Francisco, CA 94158, USA*

### ABSTRACT

We construct the first physics-informed neural-network (PINN) surrogates for relativistic magnetohydrodynamics (RMHD) using a hybrid PDE and data-driven workflow. Instead of training for the conservative form of the equations, we work with Jacobians or PDE characteristics directly in terms of primitive variables. We further add to the trainable system the divergence-free condition, without the need of cleaning modes. Using a novel MUON optimizer implementation, we show that a baseline PINN trained on early-time snapshots can extrapolate RMHD dynamics in one and two spatial dimensions, and that posterior residual-guided networks can systematically reduce PDE violations.

### 1. INTRODUCTION

Electromagnetic observations of various astrophysical phenomena are described by emission from relativistic plasmas. Accurate descriptions of these systems are necessary to answer longstanding questions in astronomy, such as, how a galaxy’s structure is influenced by its central supermassive black hole Cho et al. (2025); Kramer, Joana A. et al. (2024), how supermassive black holes grow and evolve Ricarte et al. (2023), and the mechanisms behind pulsar and quasar emission McKinney (2006); Ighina et al. (2025). In many of these systems, the bulk flow of the plasma can reach relativistic speeds, and is well described as a conducting fluid whose motion is constrained by the presence of a magnetic field. The framework that describes these assumptions is that of Relativistic magnetohydrodynamics (RMHD).

RMHD reduces to the case of ideal RMHD when plasmas are assumed to have negligible resistivity. The governing equations for ideal RMHD are a set of eight hyperbolic first order partial differential equations (PDEs) with an elliptic constraint. The structure of these equations permits the application of various conservative schemes for generating solutions (Toro 2009a), which are necessary to accurately capture shocks that arise generically during evolution. These schemes, however, all feature characteristic deficiencies which they must overcome. Firstly, the requirement of consistency with relativity requires the definition of suitable inversion algorithms between primitive and conserved quantities Noble et al. (2006). There is no unique way to define this inversion, with many approaches incapable of guaran-

teeing convergence. Secondly, the constraint equations impose an additional requirement that must be handled independently from how the set of hyperbolic PDEs are solved. Lastly, the conditions that determine numerical convergence are decided at the beginning of a simulation run, and cannot be changed to improve convergence after a solution has been generated.

Several conservative schemes for RMHD have been proposed with different levels of accuracy, (see e.g. Porth et al. 2017; Gammie et al. 2003; Sadowski et al. 2013). Such schemes are plagued by high computational expense that imposes practical limitations on reaching numerical convergence. For example, many schemes require the implementation of artificial numerical floors to control for low-plasma density regions (see for example Chael 2024) and are inadequate for handling deviations from the case of ideal RMHD due the stiffness imposed by additional terms (Ripperda et al. 2019). An inherent flaw to such schemes is that their accuracy is determined from the initial set-up, which prevents future corrections once approximate solutions are generated.

Machine learning methods could deliver the potential means to generate accurate solutions to these equations more efficiently. The current advent of physics-informed neural-networks (PINNs), powered by advances in neural network architecture and optimization techniques propose an appealing alternative to existing conservative schemes. PINNs have been successfully applied to non-relativistic MHD problems (Bard & Dorelli 2021; Dimitropoulos et al. 2025), RHD problems (Ferrer-Sánchez

et al. 2024), as well as a wide class of non-linear PDE systems (Raissi et al. 2019; Wang et al. 2023b).

Motivated by this, in this work we explore the implementation of a RMHD solver through PINNs. Our method addresses some of the downfalls of traditional conservative schemes. Using a state-of-the-art optimizer scheme (MUON) our method is able to achieve convergence to high precision through continuous training, and to solve for primitive quantities directly by bypassing the inversion scheme necessary for traditional integrators to work. Through hyperparameter search we find a suitable architecture to be trained in diverse RMHD tests in one and two dimensions. Furthermore, in order to guarantee convergence of the network we implement a data driven training during early times, and a PDE/residual training at late times.

## 2. FROM CONSERVATIVE SCHEME TO CHARACTERISTICS

The equations of ideal-RMHD follow from stress-energy conservation, mass-current conservation, and Maxwell's equations under the ideal-MHD condition of no electric field in the frame of the fluid. They are a set of 8 hyperbolic PDEs with an additional parabolic constraint equation. They are often written in the form,

$$\partial_t \mathcal{U}^a(\mathcal{P}) + \partial_i \mathcal{J}^{a i}(\mathcal{P}) = 0, \quad (1)$$

$$\partial_i B^i = 0. \quad (2)$$

The first term corresponds to the conserved variables,

$$\mathcal{U} = (D, \varepsilon, m_i, B_i), \quad (3)$$

which are the relativistic mass density in the laboratory frame ( $D$ ), the total energy density ( $\varepsilon$ ), momentum density ( $m_i$ ), and the laboratory frame magnetic field, ( $B^i$ ). The  $\{i, j, \dots\}$  indexes range over  $\{x, y, z\}$  spatial directions. We use the first half of the Latin alphabet  $a, b = 1, \dots, 8$  to index entries associated with conservative variables and primitives.

The conserved quantities are explicitly known functions of the primitives,

$$\mathcal{P} = (\rho, p, v^i, B^i). \quad (4)$$

which stand for laboratory frame density, pressure, velocity and magnetic field respectively. The explicit form of the functions  $\mathcal{U}(\mathcal{P})$  and  $\mathcal{J}(\mathcal{P})$  is well known for ideal RMHD and General Relativistic magnetohydrodynamics (GRMHD). We provide the former in a conventional notation in Appendix A. We assume an equation of state parametrized by an adiabatic index  $\Gamma$ ,

$$p = (\Gamma - 1)u \quad (5)$$

where  $u$  is the internal energy. Throughout this work different values of  $\Gamma$  will be considered.

Conservative schemes for solving GRMHD equations are plagued by inescapable difficulties. Firstly, the function  $\mathcal{P}(\mathcal{U}) = \mathcal{U}^{-1}(\mathcal{P})$  is not bijective, and requires an iterative approach for inversion in conservative schemes. These procedures usually require the approximation of roots of high degree polynomials at every time step. Later, the function is used to obtain the currents  $\mathcal{J}^i$  which are used to approximate their flux exchange between cells of finite volume. This step is typically approximated by averaging quantities within volumes, and solving the transfer of information between cells as a Riemann problem. Another well known limitation of the system is the preservation of the divergence-free condition  $\partial_i B^i = 0$  which is crucial for proper time evolution.  
<sup>1</sup>

The computational cost of the above procedure calls for an alternative approach which bypasses the inversion scheme  $\mathcal{U} \rightarrow \mathcal{P}(\mathcal{U})$  or the strict hyperbolic requirement. Many of the difficulties associated with conservative schemes are bypassed with non-conservative schemes that avoid the evolution of conserved quantities. However, these schemes can often be unstable or lead to spurious solutions which are harder to interpret. The RMHD-NN code exploits the linear structure of the PDE system by working directly with its characteristics for the primitive variables, without reference to conserved quantities or fluxes. Indeed, we start by observing that (1) is equivalent to the following system

$$\mathcal{M}_{ab}(\mathcal{P}) \partial_t \mathcal{P}^b + \mathcal{A}_{ab}^i(\mathcal{P}) \partial_i \mathcal{P}^b = 0, \quad (6)$$

where

$$\mathcal{M}_{ab} = \frac{\partial \mathcal{U}^a}{\partial \mathcal{P}^b}, \quad \mathcal{A}_{ab}^i = \frac{\partial \mathcal{J}^{a i}}{\partial \mathcal{P}^b}. \quad (7)$$

where  $\{a, b\}$  indexes through the entries associated with each conserved quantity/primitive. The explicit form of these Jacobians is quoted in the Appendix. Schematically,  $\mathcal{M}^{-1} \mathcal{A} = \frac{\partial \mathcal{J}}{\partial \mathcal{U}}$  is the usual characteristic matrix. Positive eigenvalues reflect the hyperbolicity of the system, but can be spoiled due to failure of the constraint (2). As we will not be concerned with time evolution in our method we find this is not needed. Instead, we propose to simply augment the system (6) to 9 equations, the last one being purely spatial, the divergence-free constraint, improving convergence.

In general, the characteristics of MHD systems are physically relevant for the following reason (see, e.g., Antón (2008); Antón et al. (2010); Schoepe et al. (2018);

<sup>1</sup> See, e.g., Owkes (2024); Toro (2009b) for an introductory outline of numerical CFD methods.

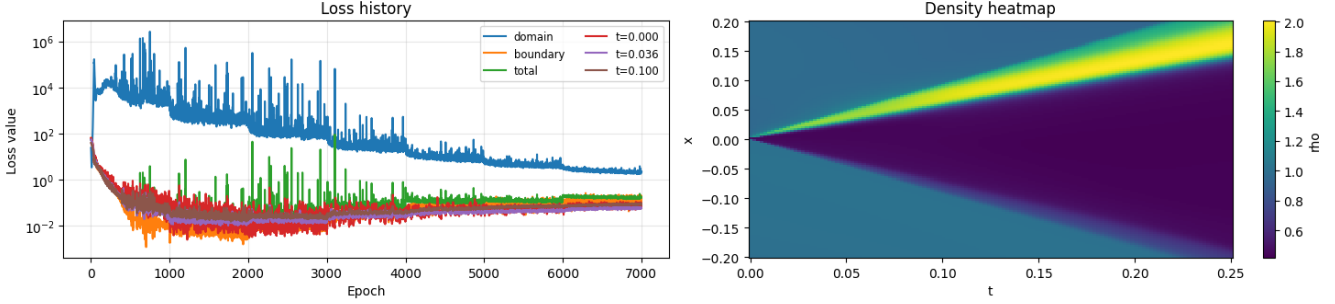


**Figure 1.** Representative 1D training process for 1D RMHD shocktube. The left panel shows the training convergence of the total loss function (green) and its weighted constituents — contributions from the boundary condition (orange) and data loss at times  $t=0.0$  (red),  $t=0.036$  (purple) and  $t=0.10$  (brown). The unweighted domain loss (blue) is also shown. The right panel shows the mass density  $\rho$  over the domain as predicted by the model.

Hilditch & Schoepe (2019); Friedrichs (1974); Anile (1989)): Linearizing the previous system around a homogeneous background, and keeping only derivative terms, yields

$$\mathcal{M}_{ab}(\mathcal{P}) \partial_t \delta \mathcal{P}^b + \mathcal{A}_{ab}^i(\mathcal{P}) \partial_i \delta \mathcal{P}^b \approx 0 \quad (8)$$

which admits a wave solution,  $\delta \mathcal{P} \propto \exp(i\omega t + ik^i x_i)$ , whose characteristic speeds are the eigenvalues of  $\mathcal{M}^{-1} \mathcal{A}_i k^i$ . The hyperbolic nature of the system is reflected in a “7-wave fan” of characteristics propagating at different rates. For instance, the Alfvén family provides an important diagnostic: the Alfvén speed (not to be confused with fluid speed)

$$v_A^2 = \frac{b^2}{b^2 + \rho h} \quad (9)$$

depends on the magnetic-field energy density  $b^2$  in the fluid frame

$$b^2 = \frac{B_i B^i}{\gamma^2} + (v_i B^i)^2 \quad (10)$$

where  $\gamma$  is the Lorentz factor and  $\rho h = \rho + \Gamma u$  is the enthalpy, as detailed in Appendix A. Correctly reproducing these characteristics is a consistency check for the RMHD implementation. Note that extra waves can also emerge in some circumstances due to artificially enforcing the constraint (2), see Dedner et al. (2002), but in our setup it will not be necessary.

### 3. PHYSICS-INFORMED NEURAL NETWORKS FOR RMHD

Here, we detail the network architecture and training schedule used for our experiments.

#### 3.1. Architecture

We represent the primitive variables by a neural surrogate,

$$(x^\mu) \mapsto \mathcal{P}(x^\mu) = (\rho(x^\mu), p(x^\mu), v^i(x^\mu), B^i(x^\mu)). \quad (11)$$

where  $x^\mu = (t, x^i)$ . In practice this is a fully connected multilayer perceptron (MLP) with different widths and depths for 1D and 2D tests. A final exponential layer is also included to normalize  $p$  and  $u$  to be positive and  $v^2 < 1$ . In the 1D case we use about 24 layers with width 64; in 2D we use about 64 layers with width 128. The nonlinearities are trainable hyperbolic tangents Jagtap et al. (2020). For general background on variational PINNs see, e.g., Kharazmi et al. (2020).

The total loss is a weighted sum which reads, schematically,

$$L_{\text{tot}} = w_1 L_{\text{domain}} + w_2 L_{\text{data}} + w_3 L_{\text{bdy}}, \quad (12)$$

where:

- $L_{\text{domain}}$ , namely **domain PDE loss**, measures the RMHD Jacobian residual, evaluated at random spacetime collocation points. The residual is built directly from the L2 norm of (6) at the points (MSE). Note that  $\partial_i \mathcal{P}$  includes  $\partial_i B_j$ , thus we can augment this equation by the divergence-free condition (2) without extra compute. This will increase the accuracy of the solver.
- $L_{\text{data}}$  is the L2 norm fitting early-time simulation snapshots supplied in the `data1d` and `data2d` folders. This includes the initial slice at  $t = 0.0$  which would be the standard data in the initial value problem.
- $L_{\text{bdy}}$  enforces open boundary conditions by penalizing deviations of  $\mathcal{P}(x, t)$  from constant-in-time boundary values. In practice this means to preserve the boundary conditions that were imposed at  $t = 0.0$ .

We find that supplying the early time data, and not just the  $t = 0.0$  snapshot, helps drive the early training towards the correct minimum of the PDE and not just a local one. As has been observed many times with

PINNs, not enforcing initial conditions strongly enough leads to essentially trivial solutions  $\mathcal{P}^a \approx 0$  which only minimize the domain loss.

Once the baseline PINN fits the initial data accurately, it extrapolates the shock evolution to later times where no data are given and the training signal is entirely from the domain PDE residual. We refer to this process as *tradeoff between fitting and extrapolation*, in direct analogy with the well known bias-variance tradeoff, which will be exemplified explicitly in the following numerical experiments.

### 3.2. Training

Previous studies have suggested that training benefits from learning scheduling which initially bias boundary data and initial data (Wang et al. 2023a). We implement such a training regimen, by dynamically increasing the PDE weight  $w_1$  every  $\sim 10^3$  epochs. We also increase the number of domain collocation points and decrease the learning rate to control for stochastic behavior in the loss function. To prevent over-fitting, we randomly re-sample the domain, boundary and data slices on each epoch. Finally, we use the MUON optimizer (Martens et al. 2024), which we find during our tests to produce the fastest training in comparison to LBFGS and ADAM (Liu & Nocedal 1989; Kingma & Ba 2017).

A representative such training process is illustrated in Figure 1. We note that our training schedule artificially causes the total loss to increase even though the network actually learns the solution over the course of training (see Figure 2 for an illustrative example). Our main focus is the loss of the unweighted PDE loss function which enables the network to have better extrapolation.

## 4. NUMERICAL EXPERIMENTS

Here we will examine the convergence of the code for various classic tests of RMHD. Various 1D and 2D problems exhibit shockwaves characteristic of the dispersion relations of MHD. The tests we run are surveyed in Nagataki (2009).

### 4.1. 1D shocktube

Our preliminary test is the 1D shock-tube test. It features a pressure gradient propagating in both directions at different velocities. Early-time data are supplied at

$$t = 0.0, 0.036, 0.1, \quad (13)$$

and used only in  $L_{\text{data}}$ . We will use the ideal gas EOS with

$$\Gamma = 5/3 \quad (14)$$

Further initial data is described by Table 1.

**Table 1.** Initial conditions (primitive variables) for the 1D RMHD shock-tube at  $t = 0$ .

Region	$\rho$	$v^x$	$v^y$	$v^z$	$B^y$	$B^z$	$p$	$B^x$
Left	1.0	0	0	0	6.0	6.0	30	5.0
Right	1.0	0	0	0	0.7	0.7	1.0	5.0

The adaptation of the code for a 1D problem, rather than a 2D problem is straightforward, we simply proceed to mask the  $x$ -components of the velocity and magnetic fields. We set the constant

$$B_x = 5.0 \quad (15)$$

In the 1D case, this satisfies the divergence constraint (2) trivially.

Training the 1D RMHD problem provides a good illustration of the tradeoff between fitting and extrapolation. Once the baseline initial data is fitted, gradually tuning the weights loosens the fit but extrapolates the shock evolution to later times  $\sim 0.25$  (where no data are given) and the training signal is entirely from the PDE residual. The model then provides a genuine prediction that can be contrasted with non-training data. This is depicted in Figure 2.

On the other hand, figure 1 shows a typical training history and a snapshot of the  $B_y$  profile. Based on the  $x - t$  evolution plot, we find that the model is able to reproduce 6 of the RMHD characteristics. Using the results at  $t = 0.25$  and the relation (9), we can estimate the propagation of the Alfvén shock to be

$$v_A \approx 0.82 \quad (16)$$

in good agreement with the outer shockwave estimated from the  $x - t$  plot in Figure 1.

Next we analyze the outcome of two-dimensional tests.

### 4.2. 2D cylindrical explosion

In two spatial dimensions we consider a cylindrical explosion in a magnetized background. This is a signature RMHD test which in our case will assess the model capacity to reproduce a cylindrically symmetric solution (such symmetry is not imposed by the network). An initially over-pressurized circular region expands into a magnetized background, generating an outward-moving shock. The initial setup is described in the table below.

Compared to the 1D test, the network uses a deeper (64 layers) and wider (128 nodes) MLP with trainable tanh activations. Training follows the same staged schedule: early-time data fitting, followed by an increasing emphasis on the PDE residual.

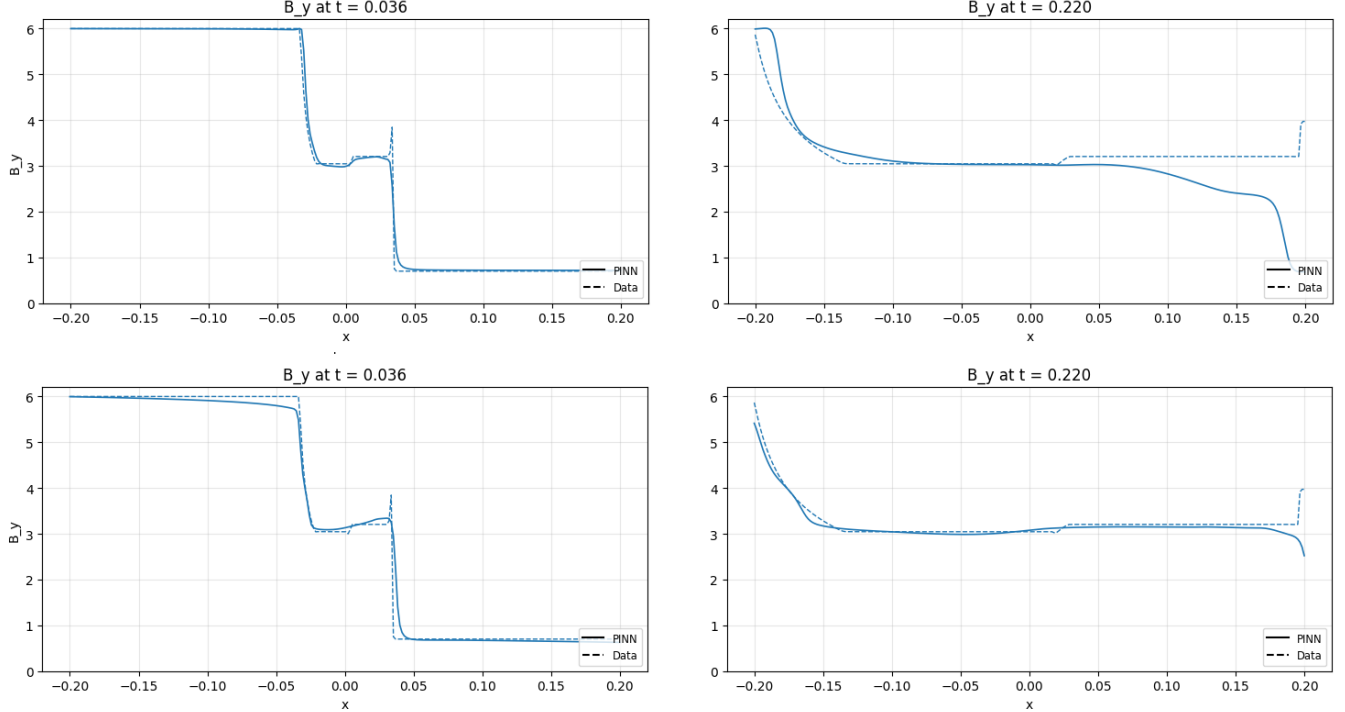
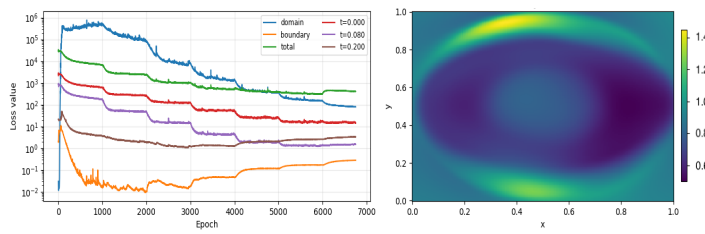


**Figure 2.** A tradeoff between fitting and extrapolating. The two upper panels shows the network prediction early into training ( $\sim 1000$  epochs). We see good fitting of data conditions at  $t=0.036$  (upper-left) and poor extrapolation to  $t=0.22$  (upper-right). The bottom two panels shows how the networks behaviour changes as the training progresses ( $\sim 7000$  epochs). Now, the quality of the network's fit to the data conditions slightly loosen, but the networks extrapolation quality increases.

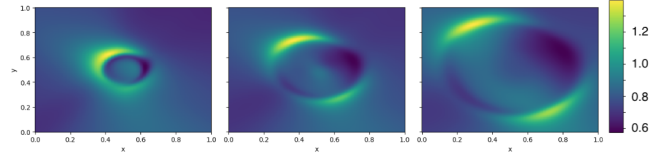
**Table 2.** Initial Conditions for 2D RMHD Cylindrical Blast Explosion

Region	$\rho$	$p$	$v^x$	$v^y$	$B^x$
Background	1.0	0.01	0	0	4.0
Blast (inside $r \leq 0.08$ )	1.0	$10^3$	0	0	4.0

Note.—Cylindrical blast centered at  $(0.5, 0.5)$  on a  $[0, 1] \times [0, 1]$ . Initial data is simulated on a grid with  $250 \times 250$  points. The equation of state uses  $\Gamma = 4/3$ . Final time is  $t = 0.4$ .



**Figure 3.** 2D cylindrical test. The left panel shows the evolution of the loss functions during training. Shown are the total loss function (green), the weighted boundary loss (orange), the weighted data losses at times  $t=0.0$  (red),  $t=0.080$  (purple) and  $t=0.20$  (brown), and the unweighted PDE loss (blue). The right panel is a heatmap of our PINN's prediction of the density at  $t = 0.40$ . We refer to the RMHD-NN repository for more details.



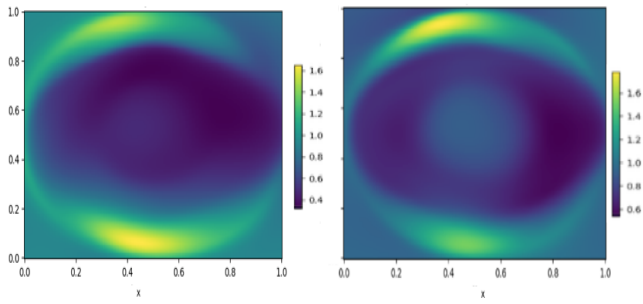
**Figure 4.** Density levels for 2D cylindrical explosion test. Model snapshots at  $t=0.0$  (left),  $t=0.2$  (middle) and  $t=0.4$  (right).

Figure 3 shows an example of the 2D loss evolution during training. Figure 4 shows a representative snapshot of the cylindrical explosion.

*Divergence free condition.* Crucially, we find that imposing the divergence free constraint (2) as an extra PDE term significantly improves the resolution of this test, see Figure 5.

### 4.3. 2D shock tube

As a final example we consider the 2D shock tube problem in relativistic hydrodynamics (RHD). This setup shows versatility of the 2D code to adapt to hydrodynamic problems in the absence of magnetism,  $B_i = 0$ . We use the same parameters and network as in the cylinder explosion, but in this case the domain is parti-



**Figure 5.** Comparison before (left) and after (right) imposing  $\partial_i B^i = 0$  constraint. We find that the constraint not only increases convergence but helps resolve the internal shock.

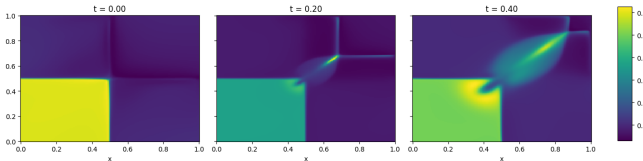


**Figure 6.** 2D shocktube tube (pressure) reconstructed from the same architecture as the cylindrical test. The evolution shows a rarefaction oblique fan where the pressure decompresses. Model snapshots at  $t=0.0$  (left),  $t=0.2$  (middle) and  $t=0.4$  (right).

tioned into four quadrants with sharp discontinuities in between.

The expectation is that each interface generates a wave fan, but because interfaces meet at right angles, the resulting waves intersect and refract.

Note that  $\Gamma$  in the equation of state is set to  $5/3$ . Final time is again set to  $0.4$ , with training data at  $t = 0, t = 0.08$  and  $t = 0.2$ . The details of the initial conditions per quadrant are given in Table 3.

**Table 3.** Initial Conditions for 2D Shock Tube Problem

Region	$x$	$y$	$\rho$	$p$	$v^x$	$v^y$
A	$0 \leq x \leq 0.5$	$0.5 \leq y \leq 1$	0.1	1	0.99	0
B	$0.5 \leq x \leq 1$	$0.5 \leq y \leq 1$	0.1	0.01	0	0
C	$0 \leq x \leq 0.5$	$0 \leq y \leq 0.5$	0.5	1	0	0
D	$0.5 \leq x \leq 1$	$0 \leq y \leq 0.5$	0.1	1	0	0.99

As expected in the absence of electromagnetism, we find the network training converges extremely well in this case, reaching accuracies of  $10^{-1}$  during a 90 minute training on a single GPU, see Figure 4.

## 5. RESIDUAL-GUIDED CORRECTION NETWORKS

Residual networks have recently emerged as a surrogate method to increase accuracy Wang et al. (2025).

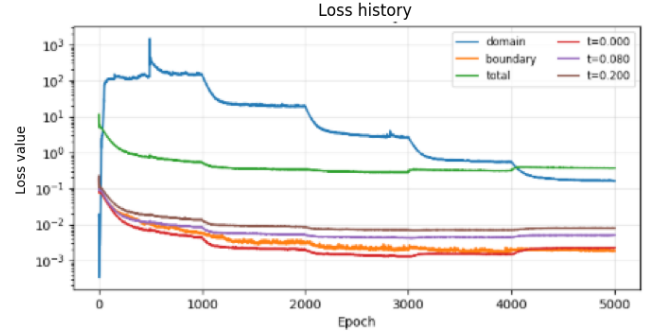


**Figure 7.** Training convergence of the 2D shocktube (note total loss is not normalized).

They are based on a linearized version of the PDE, which in our case appears natural since it corresponds to well-known characteristics of MHD systems Teukolsky (2025).

After the baseline model has converged, we evaluate the RMHD Jacobian residual on a new set of collocation points and construct a sampling density biased toward regions of large residual. For instance, in 1D we evaluate/store the residual

$$\mathcal{R}^a(\mathcal{P}) = \mathcal{M}^a_b(\mathcal{P}) \partial_t \mathcal{P}^b + A_{bx}^a(\mathcal{P}) \partial_x \mathcal{P}^b \quad (17)$$

and construct a training set of points through Monte Carlo sampling, see Figure 8. This set of points is used to define a second network,

$$(x, t) \longrightarrow \delta\mathcal{P} = (\delta\rho(x^\mu), \delta p(x^\mu), \delta v^i(x^\mu), \delta B^i(x^\mu)) \quad (18)$$

which learns an Alfvén-like perturbation that partially compensates PDE violations.

At each collocation point we treat  $\delta\mathcal{P}$  as satisfying the linearized inhomogeneous system

$$\mathcal{M}^a_b(\mathcal{P}) \partial_t \delta\mathcal{P}^b + \mathcal{A}_{bx}^a(\mathcal{P}) \partial_x \delta\mathcal{P}^b + \mathcal{S}^a_b(\mathcal{P}) \delta\mathcal{P}^b = \mathcal{R}^a(\mathcal{P}), \quad (19)$$

where  $\mathcal{P}$  denotes the background solution from the baseline PINN,  $\mathcal{M}$  is the time Jacobian,  $A_x$  the spatial Jacobian, and  $\mathcal{S}(\mathcal{P}) = \partial_t \mathcal{M}(\mathcal{P}) + \partial_x \mathcal{A}_x(\mathcal{P})$ . The correction network is trained to minimize the mismatch between the two sides of the above equation, ensuring that the corrected surrogate  $\mathcal{P} - \delta\mathcal{P}$  better satisfies the Jacobian-form PDE. This is depicted in Fig. 9.

## 6. DISCUSSION AND OUTLOOK

The RMHD-NN framework combines a primitive-variable Jacobian formulation of RMHD with standard PINNs, an aggressive optimizer schedule, and residual-guided correction stages. In the current tests (1D shock tube and 2D cylindrical explosion) the method:

1. reproduces RMHD dynamics from limited early-time data,

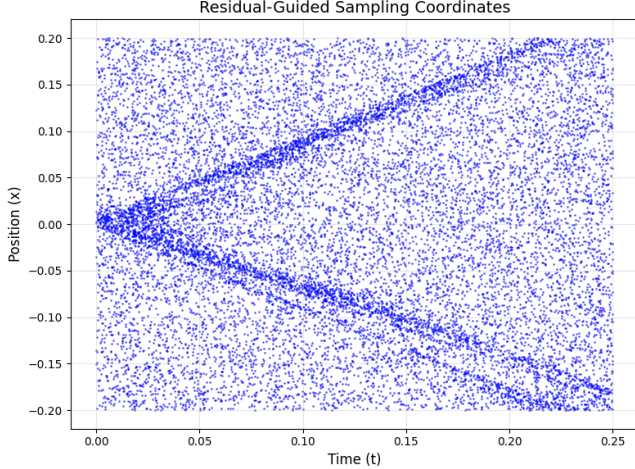


**Figure 8.** Monte-Carlo sampling for the 1D shock-tube test. Points are concentrated where the Jacobian residual is largest.

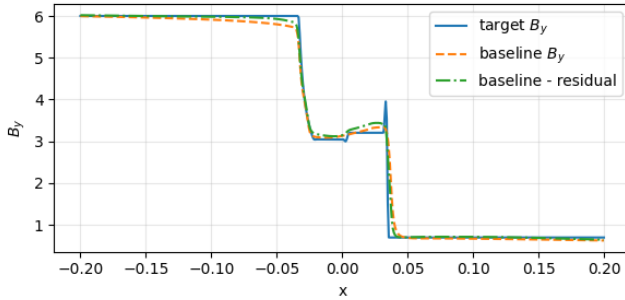


**Figure 9.** Residual output after 5000 training steps, illustrating the residual-guided correction.

2. extrapolates to later times using only PDE information,
3. systematically reduces residuals via correction networks.

Alternative methods of achieving the last point shall also be explored in the future.

The next step in this direction is the implementation of PINN model for GRMHD equations supported on a curved spacetime, where a rotating black hole is of special interest. In this case initial data with early time simulation is harder to generate, but there exists well known libraries. Furthermore, in real world GRMHD applications, the models serve as a prior in Bayesian methods, and one is only required to achieve the accuracy levels within the measurement expectations.

We find it very promising that the overall time of training does not exceed  $\sim 90$  minutes in a single GPU. This suggests perhaps the network can be escalated to higher accuracy. In doing so the role of an optimizer

like MUON is crucial, with alternatives including heavier Gauss-Newton methods [Wang et al. \(2025\)](#).

Other natural extensions of our implementation include more than one correction stages, iterating the residual-guided procedure.

A more systematic study of stability, generalization, and comparison to traditional RMHD schemes is left for future work.

## ACKNOWLEDGEMENTS

This project was partially funded through the Harvard College Research Program (HCRP). We further thank Harvard Research Computing (HRC) for availability of computing resources. We especially thank Richard Qiu for collaboration and guidance at the beginning stages of this project. We thank Mark Goldstein for further discussions and for suggesting the application of a MUON optimizer. Simulation of initial/early time data was done using the Black Hole Accretion Code (BHAC) which is publicly available in [Porth et al. \(2017\)](#). This publication is funded in part by the Gordon and Betty Moore Foundation, Grant GBMF12987. This work was supported by the Black Hole Initiative, which is funded by grants from the John Templeton Foundation (Grant #62286) and the Gordon and Betty Moore Foundation (Grant GBMF-8273) — although the opinions expressed in this work are those of the authors) and do not necessarily reflect the views of these Foundations.

This write-up is based on our publicly available RMHD-NN code repository, see <https://github.com/aguevara22/RMHD-NN>.

## APPENDIX

## A. RMHD EQUATIONS AND JACOBIANS

In this Appendix we list the explicit form of the RMHD equations and its Jacobians. The RMHD equations model a plasma in fluid state interacting with an electromagnetic field. As such, we fundamentally have three first order constraints for evolution. In relativistic notation these are  $\partial_\mu \mathcal{T}^{\mu\nu} = 0$ ,  $\partial_\mu F^{\mu\nu} = 0$  and  $\partial_\mu (\epsilon^{\mu\nu} \rho_\sigma F^{\rho\sigma}) = 0$ , where  $\mathcal{T}^{\mu\nu}$  is the stress-energy tensor,  $F^{\mu\nu}$  is the Maxwell tensor, and  $\epsilon^{\mu\nu\rho\sigma}$  is the Levi-Civita symbol. These equations each correspond to stress-energy conservation (of a perfect-fluid and electromagnetic 4-momentum), Gauss' law and Ampere's law, and the no-monopole condition and Faraday's law. The second equation is typically approximated with an Ohmic relationship,  $J^\mu = \sigma_{\mu\nu} F^{\mu\nu}$  where  $\sigma^{\mu\nu}$  is the conductivity tensor. The equations simplify drastically in an 'ideal' MHD scenario, namely the condition of infinite conductivity (zero-resistivity). The ideal-MHD condition is equivalent to  $F^{\mu\nu} U_\nu = 0$  where  $U_\nu$  is a relativistic 4-velocity, representing the absence of the electric field in the plasma frame.

The full RMHD system is obtained by grouping together time and spatial derivative in the above equations. In this appendix we will switch to a more conventional notation to describe (1). We will use bolded notation for three-vectors  $\mathbf{v} = \{v^i\}$  and dyadics  $\mathbf{ab} = \{a^i b^j\}$ . In this form we have,

$$\frac{\partial}{\partial t} \begin{pmatrix} D \\ \mathbf{m} \\ \varepsilon \\ \mathbf{B} \end{pmatrix} + \nabla \cdot \begin{pmatrix} D\mathbf{v} \\ w_t \gamma^2 \mathbf{v} \mathbf{v} - \mathbf{b} \mathbf{b} + \mathbf{I} p_t \\ \mathbf{m} \\ \mathbf{v} \mathbf{B} - \mathbf{B} \mathbf{v} \end{pmatrix}^T = \begin{pmatrix} 0 \\ \mathbf{0} \\ 0 \\ \mathbf{0} \end{pmatrix}. \quad (\text{A1})$$

With these equations, we define the conserved quantities,

$$\begin{aligned} D &= \gamma \rho \\ \mathbf{m} &= w_t \gamma^2 \mathbf{v} - b^0 \mathbf{b} \\ \varepsilon &= w_t \gamma^2 - b^0 b^0 - p_t \end{aligned} \quad (\text{A2})$$

involving the following functions,

$$\begin{aligned} b^0 &= \gamma \mathbf{v} \cdot \mathbf{B} \\ \mathbf{b} &= \mathbf{B}/\gamma + \gamma(\mathbf{v} \cdot \mathbf{B}) \mathbf{v} \\ w_t &= \rho h + b^2 \\ p_t &= p + \frac{b^2}{2} \\ \gamma &= 1/\sqrt{1 - v^2}, \quad v^2 := v_x^2 + v_y^2 + v_z^2. \end{aligned} \quad (\text{A3})$$

The currents/fluxes  $\mathbf{J}^a$  correspond to a  $3 \times 8$  matrix, with  $a = 1, \dots, 8$ . For instance

$$\mathbf{J}^1 = D\mathbf{v}, \quad \mathbf{J}^2 = w_t \gamma^2 \mathbf{v} v_x - \mathbf{b} b_x + \hat{\mathbf{i}} p_t, \quad \mathbf{J}^3 = \dots \quad (\text{A4})$$

etc. Recall that  $\gamma$  is the Lorentz factor of the plasma and that  $b^\mu = (b^0, \mathbf{b})$  is the magnetic field in such frame. This yields the useful identity for the 4-norm  $b^2 \equiv b^\mu b_\mu$ ,

$$b^2 = \mathbf{B}^2 / \gamma^2 + (\mathbf{v} \cdot \mathbf{B})^2 \quad (\text{A5})$$

For completeness we further summarize the Jacobian formulation used throughout this work. We adopt the primitive variables

$$P = (\rho, v_x, v_y, v_z, B_x, B_y, B_z, p). \quad (\text{A6})$$

The Jacobian matrices used in the code (Eq. (3)) are given by

$$M^{ab} = \frac{\partial U^a}{\partial P^b}, \quad \mathbf{A}^{ab} = \frac{\partial \mathbf{J}^a}{\partial P^b} \quad (\text{A7})$$

where  $a, b = 1, \dots, 8$  and  $\mathbf{A} = (A^x, A^y, A^z)$ . For illustration purposes we quote here the explicit form of the full  $8 \times 8$  matrix  $M$ . Recalling the enthalpy of the  $\Gamma$ -gas

$$\rho h = \rho + p + u, \quad p = (\Gamma - 1)u \quad (\text{A8})$$

we find

$$M(P) = \begin{pmatrix} \gamma & \gamma^3 \rho v_x & \gamma^3 \rho v_y & \gamma^3 \rho v_z & 0 & 0 & 0 & 0 \\ \gamma^2 v_x & h\gamma^2 + B^2 - B_x^2 + 2h\gamma^4 v_x^2 & -B_x B_y + 2h\gamma^4 v_x v_y & -B_x B_z + 2h\gamma^4 v_x v_z & -B_y v_y - B_z v_z & 2B_y v_x - B_x v_y & 2B_z v_x - B_x v_z & \frac{\Gamma \gamma^2 v_x}{\Gamma - 1} \\ \gamma^2 v_y & -B_x B_y + 2h\gamma^4 v_x v_y & h\gamma^2 + B^2 - B_y^2 + 2h\gamma^4 v_y^2 & -B_y B_z + 2h\gamma^4 v_y v_z & -B_y v_x + 2B_x v_y & -B \cdot v + B_y v_y & 2B_z v_y - B_y v_z & \frac{\Gamma \gamma^2 v_y}{\Gamma - 1} \\ \gamma^2 v_z & -B_x B_z + 2h\gamma^4 v_x v_z & -B_y B_z + 2h\gamma^4 v_y v_z & h\gamma^2 + B_x^2 + B_y^2 + 2h\gamma^4 v_z^2 & -B_z v_x + 2B_x v_z & -B_z v_y + 2B_y v_z & -B \cdot v + B_z v_z & \frac{\Gamma \gamma^2 v_z}{\Gamma - 1} \\ 0 & 0 & 0 & 0 & 1 & 0 & 0 & 0 \\ 0 & 0 & 0 & 0 & 0 & 1 & 0 & 0 \\ 0 & 0 & 0 & 0 & 0 & 0 & 1 & 0 \\ \gamma^2 & -(B \cdot v) B_x + (B^2 + 2h\gamma^4) v_x & -(B \cdot v) B_y + (B^2 + 2h\gamma^4) v_y & -(B \cdot v) B_z + (B^2 + 2h\gamma^4) v_z & B_x \left(2 - \frac{1}{\gamma^2}\right) - (B \cdot v) v_x & B_y \left(2 - \frac{1}{\gamma^2}\right) - (B \cdot v) v_y & B_z \left(2 - \frac{1}{\gamma^2}\right) - (B \cdot v) v_z & -1 + \frac{\Gamma \gamma^2}{\Gamma - 1} \end{pmatrix}$$

The matrices  $A^x(P)$  and  $A^y(P)$  are also  $8 \times 8$ , we refer the reader to the exact definitions in our publicly available code `jacobians.py`. For computational efficiency they are computed via symbolic differentiation using the software `Mathematica`, but can be shown to match, numerically and precisely, with the backpropagating gradient of the `pytorch` environment (obtained from their definition (A7)).

All together, this system determines the characteristic speeds of the linearized RMHD system via the eigenvalues of  $M^{-1} A^a k^a$ , which include the relativistic fast/slow magnetosonic and Alfvén families.

## REFERENCES

- Anile, A. M. 1989, Relativistic Fluids and Magneto-Fluids: With Applications in Astrophysics and Plasma Physics (New York: Cambridge University Press)
- Antón, L. 2008, PhD thesis, Universitat de València
- Antón, L., Miralles, J. A., Martí, J. M., et al. 2010, Astrophysical Journal Supplement Series, 188, 1. <https://arxiv.org/abs/0912.4692>
- Bard, C., & Dorelli, J. C. 2021, Front. Astron. Space Sci., 8
- Chael, A. 2024, Monthly Notices of the Royal Astronomical Society, 532, 3198, doi: [10.1093/mnras/stae1692](https://doi.org/10.1093/mnras/stae1692)
- Cho, H., Prather, B. S., Narayan, R., Su, K.-Y., & Natarajan, P. 2025, arXiv e-prints, arXiv:2507.17818, doi: [10.48550/arXiv.2507.17818](https://doi.org/10.48550/arXiv.2507.17818)
- Dedner, A., Kemm, F., Kröner, D., et al. 2002, Journal of Computational Physics, 175, 645, doi: [10.1006/jcph.2001.6961](https://doi.org/10.1006/jcph.2001.6961)
- Dimitropoulos, I., Chaniadakis, E., & Contopoulos, I. 2025, Astronomy & Astrophysics. <https://arxiv.org/abs/2410.10716>
- Ferrer-Sánchez, A., Martín-Guerrero, J. D., Ruiz de Austri-Bazán, R., Torres-Forné, A., & Font, J. A. 2024, Computer Methods in Applied Mechanics and Engineering, 424, 116906, doi: [10.1016/j.cma.2024.116906](https://doi.org/10.1016/j.cma.2024.116906)
- Friedrichs, K. O. 1974, Communications on Pure and Applied Mathematics, 27, 749
- Gammie, C. F., McKinney, J. C., & Toth, G. 2003, *Astrophys. J.*, 589, 444. <https://arxiv.org/abs/astro-ph/0301509>
- Hilditch, D., & Schoepe, A. 2019, *Physical Review D*, 99, 104034
- Ighina, L., Caccianiga, A., Connor, T., et al. 2025, *The Astrophysical Journal Letters*, 990, L56, doi: [10.3847/2041-8213/aded0a](https://doi.org/10.3847/2041-8213/aded0a)
- Jagtap, A. D., Kawaguchi, K., & Karniadakis, G. E. 2020, *Journal of Computational Physics*, 404, 109136, doi: [10.1016/j.jcp.2019.109136](https://doi.org/10.1016/j.jcp.2019.109136)
- Kharazmi, E., Zhang, Z., & Karniadakis, G. E. 2020, arXiv preprint arXiv:2001.04536. <https://arxiv.org/abs/2001.04536>
- Kingma, D. P., & Ba, J. 2017, Adam: A Method for Stochastic Optimization. <https://arxiv.org/abs/1412.6980>
- Kramer, Joana A., MacDonald, Nicholas R., Paraschos, Georgios F., & Ricci, Luca. 2024, *A&A*, 691, A14, doi: [10.1051/0004-6361/202450978](https://doi.org/10.1051/0004-6361/202450978)
- Liu, D. C., & Nocedal, J. 1989, *Math. Program.*, 45, 503
- Martens, J., Zhang, M., Chen, X., et al. 2024, arXiv preprint arXiv:2405.21055. <https://arxiv.org/abs/2405.21055>
- McKinney, J. C. 2006, *MNRAS*, 368, L30, doi: [10.1111/j.1745-3933.2006.00150.x](https://doi.org/10.1111/j.1745-3933.2006.00150.x)

- Nagataki, S. 2009, *Astrophys. J.*, 704, 937–950. <https://arxiv.org/abs/0902.1908>
- Noble, S. C., Gammie, C. F., McKinney, J. C., & Del Zanna, L. 2006, *Astrophys. J.*, 641, 626, doi: [10.1086/500349](https://doi.org/10.1086/500349)
- Owkes, M. 2024, A guide to writing your first CFD solver
- Porth, O., Olivares, H., Mizuno, Y., et al. 2017, *Comput. Astrophys. Cosmol.*, 4, 1. <https://arxiv.org/abs/1611.09720>
- Raissi, M., Perdikaris, P., & Karniadakis, G. 2019, *Journal of Computational Physics*, 378, 686, doi: <https://doi.org/10.1016/j.jcp.2018.10.045>
- Ricarte, A., Narayan, R., & Curd, B. 2023, *The Astrophysical Journal Letters*, 954, L22, doi: [10.3847/2041-8213/aceda5](https://doi.org/10.3847/2041-8213/aceda5)
- Ripperda, B., Bacchini, F., Porth, O., et al. 2019, *The Astrophysical Journal Supplement Series*, 244, 10, doi: [10.3847/1538-4365/ab3922](https://doi.org/10.3847/1538-4365/ab3922)
- Sadowski, A., Narayan, R., Tchekhovskoy, A., & Zhu, Y. 2013, *Mon. Not. Roy. Astron. Soc.*, 429, 3533. <https://arxiv.org/abs/1212.5050>
- Schoepe, A., Hilditch, D., & Bugner, M. 2018, *Physical Review D*, 97, 123009. <https://arxiv.org/abs/1712.09837>
- Teukolsky, S. A. 2025. <https://arxiv.org/abs/2511.13836>
- Toro, E. F. 2009a, *Riemann solvers and numerical methods for fluid dynamics*, 3rd edn. (Berlin, Germany: Springer)
- . 2009b, *Riemann Solvers and Numerical Methods for Fluid Dynamics: A Practical Introduction*, 3rd edn. (Berlin, Germany: Springer)
- Wang, S., Sankaran, S., Wang, H., & Perdikaris, P. 2023a, *An Expert’s Guide to Training Physics-informed Neural Networks*. <https://arxiv.org/abs/2308.08468>
- Wang, Y., Lai, C.-Y., Gómez-Serrano, J., & Buckmaster, T. 2023b, *Phys. Rev. Lett.*, 130, 244002, doi: [10.1103/PhysRevLett.130.244002](https://doi.org/10.1103/PhysRevLett.130.244002)
- Wang, Y., Bennani, M., Martens, J., et al. 2025. <https://arxiv.org/abs/2509.14185>